Materials Research Letters

ISSN: (Print) (Online) Journal homepage: https://www.tandfonline.com/loi/tmrl20

Novel single crystalline-like non-equiatomic TiZrHfNbTaMo bio-high entropy alloy (BioHEA) developed by laser powder bed fusion

Ozkan Gokcekaya, Takuya Ishimoto, Yuki Nishikawa, Yong Seong Kim, Aira Matsugaki, Ryosuke Ozasa, Markus Weinmann, Christoph Schnitter, Melanie Stenzel, Hyoung Seop Kim, Yoshitsugu Miyabayashi & Takayoshi Nakano

To cite this article: Ozkan Gokcekaya, Takuya Ishimoto, Yuki Nishikawa, Yong Seong Kim, Aira Matsugaki, Ryosuke Ozasa, Markus Weinmann, Christoph Schnitter, Melanie Stenzel, Hyoung Seop Kim, Yoshitsugu Miyabayashi & Takayoshi Nakano (2023) Novel single crystalline-like non-equiatomic TiZrHfNbTaMo bio-high entropy alloy (BioHEA) developed by laser powder bed fusion, Materials Research Letters, 11:4, 274-280, DOI: 10.1080/21663831.2022.2147406

To link to this article: https://doi.org/10.1080/21663831.2022.2147406

Published online: 29 Nov 2022.

MATER. RES. LETT.
2023, VOL. 11, NO. 4, 274–280
https://doi.org/10.1080/21663831.2022.2147406

MATERIALS RESEARCH LETTERS
Taylor & Francis
Taylor & Francis Group

ORIGINAL REPORTS

Novel single crystalline-like non-equiatomic TiZrHfNbTaMo bio-high entropy alloy (BioHEA) developed by laser powder bed fusion

Ozkan Gokcekaya [a,b], Takuya Ishimoto [a,b,c], Yuki Nishikawa[a], Yong Seong Kim[a], Aira Matsugaki [a,b], Ryosuke Ozasa [a,b], Markus Weinmann [d], Christoph Schnitter [d], Melanie Stenzel [d], Hyoung Seop Kim [e], Yoshitsugu Miyabayashi [f] and Takayoshi Nakano [a,b]

[a]Division of Materials and Manufacturing Science, Graduate School of Engineering, Osaka University, Osaka, Japan; [b]Anisotropic Design and Additive Manufacturing Research Center, Osaka University, Osaka, Japan; [c]Aluninium Research Center, University of Toyama, Toyama, Japan; [d]TANIOBIS GmbH, Goslar, Germany; [e]Department of Materials Science and Engineering, Pohang University of Science and Technology, Pohang, South Korea; [f]Graduate School of Engineering, Osaka University, Osaka, Japan

ABSTRACT

This study developed a non-equiatomic $Ti_{28.33}Zr_{28.33}Hf_{28.33}Nb_{6.74}Ta_{6.74}Mo_{1.55}$ super-solid solutionized BioHEA using laser powder bed fusion (LPBF) to reach the full potential as BioHEA. We succeeded in significant suppression of elemental segregation, thus, resulting in a single crystalline-like texture by activating layer-to-layer epitaxial growth. Relatively low Young's modulus was achieved in the single crystalline-like BioHEA. Moreover, LPBF-fabricated BioHEA exhibited significantly higher yield stress (1355–1426 MPa) due to the effective solid solution hardening compared to as-cast counterpart with marked segregation (949 MPa), and good biocompatibility. This is first report achieving BioHEA with low modulus, excellent strength-ductility balance, and good biocompatibility via LPBF.

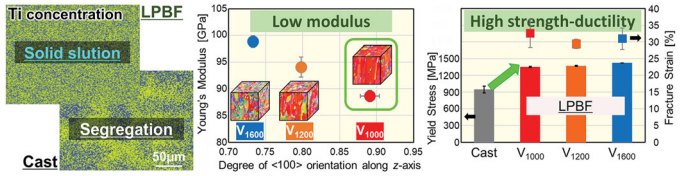

ARTICLE HISTORY
Received 7 October 2022

KEYWORDS
Laser powder bed fusion; high-entropy alloys; super solid solution; crystallographic texture; mechanical property

IMPACT STATEMENT

This study achieved super-solid-solutionized and single crystalline-like TiZrHfNbTaMo bio-high entropy alloy using laser powder bed fusion, resulting in low Young's modulus along $<001>$ oriented direction, excellent strength-ductility balance, and good cytocompatibility.

1. Introduction

Next-generation metallic biomaterials should exhibit superior mechanical performance and biocompatibility while allowing custom design for individual needs [1]. Thus, developing new metallic biomaterials with high strength, low elastic modulus, and biocompatibility is important to fulfil the demands for biomedical applications.

Recently, a new class of structural and functional materials called high-entropy alloys (HEAs) has emerged [2,3]. Our group proposed equiatomic TiNbTaZrMo HEAs for biomedical applications, defined as BioHEAs [4], which have now expanded to diverse alloy systems using biocompatible elements [4–12]. However, severe segregation and consequent phase separation are inevitable because of the super-multicomponent nature of the HEA system when general solidification methods such as casting are used. Severe segregation reduces lattice distortion that is the origin of the high functionality of HEAs [13,14]. Therefore, the occurrence of segregation means that the materials do not perform as well as HEAs.

To suppress elemental segregation and simultaneously achieve shape customisation, we proved the advantage of the laser powder bed fusion (LPBF) method. The extremely rapid cooling ($\sim 10^7$ K/s) [15] achieved during solidification in LPBF significantly inhibits diffusion and thus suppresses segregation, and promotes the

CONTACT Takayoshi Nakano nakano@mat.eng.osaka-u.ac.jp Division of Materials and Manufacturing Science, Graduate School of Engineering, Osaka University, 2-1 Yamada-oka, Suita, Osaka 565-0871, Japan

formation of a solid solution [16], which could result in an effective solid solution strengthening. Another advantage of LPBF is that crystallographic texture control is enabled and a single crystalline-like microstructure can be obtained [17,18]. For single crystalline-like texture formation, the implementation of epitaxial growth between the laser scanning tracks and layers is essential [19]. Thus, if factors that inhibit epitaxial growth are present, a single crystalline-like texture cannot be realised. β-type titanium-based materials with a BCC structure show a crystallographic orientation-dependant variation in Young's modulus, with the lowest modulus along $<001>$ [17,20]. Acquisition of single crystals is an important strategy [21] for achieving low-modulus biomaterials [22]. However, inevitable severe segregation nature due to the intrinsic fact that HEA is an ultra-multicomponent alloy system could disturb the formation of single crystalline-like texture. Elemental segregation results in a microstructure composed of multi-phases with differed melting point. The phases with high melting points can remain undissolved in the melt pool during remelting and acted as nucleation sites, inhibiting epitaxial growth from the beneath layer and preventing the formation of a single crystalline structure [23].

In this study, the principles of BioHEA creation thru LPBF fabrication are (1) suppression of elemental segregation, (2) formation of single crystalline-like prominent texture, and (3) reduction in low Young's modulus. To minimise the segregation tendency, the difference between the liquidus and solidus temperatures (ΔT) was designed to be small. Segregation inhibition promotes epitaxial growth and strong texture formation during LPBF. The reduction in electron per atom ratio (e/a) is expected to contribute to a reduced Young's modulus along the crystallographic $<001>$ direction, as reported in β-Ti alloy system. The decrease in the shear modulus for the $110<1\bar{1}0>$ shear as a function of the reduction in e/a leads to the decrease in Young's modulus along $<001>$ [20]. A low e/a which is equivalent to a low valence electron concentration (*VEC*) in this alloy system is also beneficial to improve room-temperature ductility [24,25]. Under this line, we decided to fabricate $Ti_{28.33}Zr_{28.33}Hf_{28.33}Nb_{6.74}Ta_{6.74}Mo_{1.55}$ (at. %) BioHEA with a mixing entropy of $1.5R$ (R is the gas constant) thru LPBF. For this BioHEA, ΔT estimated by thermodynamic calculations using FactSage and SGTE2017 was 50 K, which was significantly lower than the $\sim$300 K of the previously reported $Ti_{1.4}Zr_{1.4}Nb_{0.6}Ta_{0.6}Mo_{0.6}$ BioHEA with severe elemental segregation [26]. Consequently, the deviation of the distribution coefficients, which is defined as the ratio of the element's concentration in the solidus phase compared to that in the liquidus phase of each element, from 1 decreased, which was expected to reduce the tendency to segregate. *VEC* was reduced from 4.52 to 4.17, which is somewhat larger than that of Ti-15Mo-5Zr-3Al (wt. %), ISO-approved low-modulus β-Ti alloy for metallic implant materials (ISO 5832-14). To fine-tune these parameters, a nonequiatomic six-elemental alloy system was created instead of equiatomic quintette compositions that are commonly designed as HEAs.

Table 1. Overall compositions (at. %) of powder, cast and LPBF-fabricated specimens.

	Ti	Zr	Hf	Nb	Ta	Mo
Powder	28.1	28.0	28.5	6.9	6.8	1.7
Cast	27.7	28.7	28.6	6.8	6.7	1.5
LPBF	28.7	27.9	28.3	6.9	6.6	1.7

2. Materials and methods

The mostly spherical BioHEA powders (Figure 1(a)) were prepared using electrode induction melting gas atomisation of pre-alloyed rods (TANIOBIS, Germany). The powder was sieved to obtain a compatible size distribution for LPBF, resulting in an average diameter of 31.5 µm. The chemical composition of the powder, measured using the inductively coupled plasma method, is shown in Table 1. The composition was approximately the same as expected. The rest angle of the powder measured using a Revolution powder analyser (Mercury Scientific, USA) was 41.2°, which is close to that of commercial Ti-6Al-4V spherical powders (EOS, Germany) (39.2°) [27], indicating good flowability. The quality of the powders and processability of complex shapes by LPBF were demonstrated by fabricating a jungle-gym-shaped lattice structure, as shown in Figure 1(b).

To investigate the intrinsic microstructure, mechanical properties, and biocompatibility of the LPBF-processed BioHEA, cubic samples with dimensions of $5 \times 5 \times 5$ mm were fabricated using an LPBF apparatus (EOS M290, EOS) with a laser power, scan pitch, and layer thickness of 240 W, 80, and 60 µm, respectively. The laser scanning speed was varied at 1000, 1200, and 1600 mm/s to change the crystallographic texture; they were named V_{1000}, V_{1200}, and V_{1600}, respectively. The fabrication was performed under an Ar atmosphere. The scanning strategy adopted in this study was bidirectional (zigzag) scanning with a rotation of 90° between layers (Scan strategy XY), in which a cube texture with low modulus $<001>$ alined in the x-, y-, and z-directions is expected to be obtained [28]. The relative densities of the fabricated specimens were determined using field-emission scanning electron microscopy (FE-SEM; JIB-4610F, JEOL, Japan). As a control, an ingot with the same composition was prepared by arc melting.

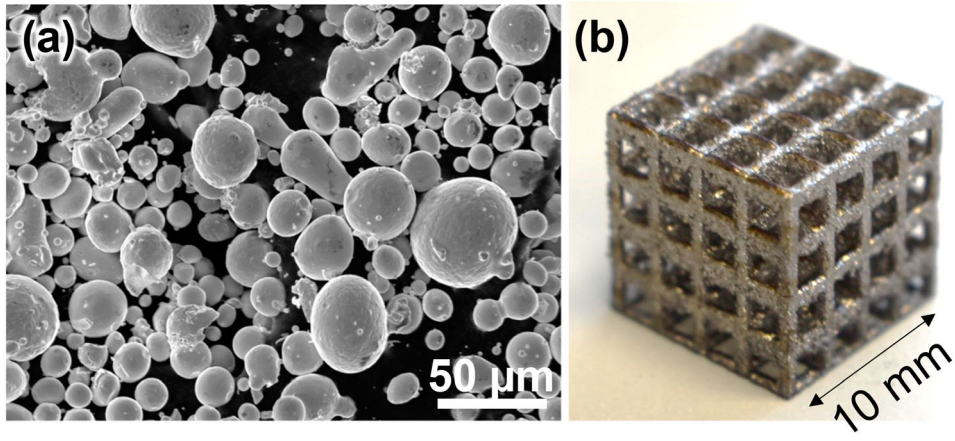

Figure 1. Powder and LPBF-built $Ti_{28.33}Zr_{28.33}Hf_{28.33}Nb_{6.74}Ta_{6.74}Mo_{1.55}$ BioHEA. (a) SEM image of gas-atomised powder and (b) appearance of LPBF-built jungle gym-shaped product.

The microstructures were analysed using an FE-SEM equipped with energy-dispersive X-ray spectroscopy (EDS, Aztec 3.1, Oxford Instruments, UK) and an electron backscatter diffraction system (EBSD; NordlysMax^3, Oxford Instruments). To quantitatively analyse the evolved texture, the degree p of 001 orientation along the build direction was calculated based on the Euler angles obtained by EBSD using the following Equation (1):

$$p_{\langle 001\rangle} = \langle \cos^2 \alpha_{\langle 001\rangle} \rangle, \quad (1)$$

where α_{001} is the angle between the observation direction and one of the equivalent orientations $< 001 >$. The maximum value of $p_{<001>}$ is 1, which represents $< 001 >$ perfectly oriented along the observation direction. To evaluate the mechanical properties of the BioHEA, rectangular test pieces with dimensions of $2 \times 2 \times 5$ mm were prepared, where the 5 mm-length side was parallel to the build direction. Compression tests ($n = 3$) were conducted using an Instron-type testing machine (AG-X, Shimadzu, Japan) at a nominal strain rate of 1.67×10^{-4} s^{-1} at room temperature. A non-contact extensometer (TRViewX, Shimadzu) was used to detect the strain and determine the Young's modulus.

A primary osteoblast culture experiment was performed according to a previously described protocol [8] to evaluate the biocompatibility of the BioHEA. Plates of $5 \times 5 \times 1$ mm ($n = 5$) were prepared, and the surface for cell culture was mirror-polished. Specimens of the same size as commercially pure Ti (CP-Ti), 316 L-type stainless steel (SUS316L), and arc-melted (as-cast) BioHEA were also prepared for comparison. Cell density was evaluated using Giemsa staining (FUJIFILM Wako Chemicals, Japan). Quantitative results are expressed as mean ± standard deviation. Statistical significance was assessed using a two-tailed unpaired t-test or one-way analysis of variance (ANOVA) followed by Tukey's post-hoc test. A p-value < 0.05 was considered statistically significant.

3. Results and discussion

All three samples prepared at different laser scanning speeds exhibited high densities of 99.92%, 99.87%, and 99.73% for specimens V_{1000}, V_{1200}, and V_{1600}, respectively. According to the X-ray diffraction analysis, only BCC peaks were detected, and no peaks corresponding to intermetallic compounds and/or BCC-based ordering structures were observed in either the cast or LPBF-fabricated specimens (data not shown). The overall compositions of the cast and LPBF-fabricated specimens are listed in Table 1 and were approximately as designed. Processing with LPBF caused little change in powder composition. Figure 2(a,b) shows the SEM-BSE images and the corresponding EDS maps of Ti, Zr, and Ta in the cast specimen and LPBF-processed specimen (V_{1000}). In the cast specimen, the compositional differences between the dendritic (bright contrast, indicated by 'D') and interdendritic (dark contrast) regions are obvious. The EDS quantitative data in Figure 2(c) clearly indicate that Ti, Zr, and Mo were enriched in the interdendritic region, and Hf, Nb, and Ta were enriched in the dendritic region in the cast specimen. This segregation tendency agrees well with the estimated distribution coefficients at the liquidus temperature using FactSage: 0.85, 0.93, 1.14, 1,13, 1.25, and 0.85 for Ti, Zr, Hf, Nb, Ta, and Mo, respectively. Elemental segregation leads to low mixing entropy, in some cases below 1.5R, and causes the alloys to deviate from the definition of HEAs. In contrast, as expected, elemental segregation was largely suppressed in the LPBF-fabricated sample compared to the cast material, indicating the realisation of a super-solid solution owing to ultrarapid cooling in LPBF.

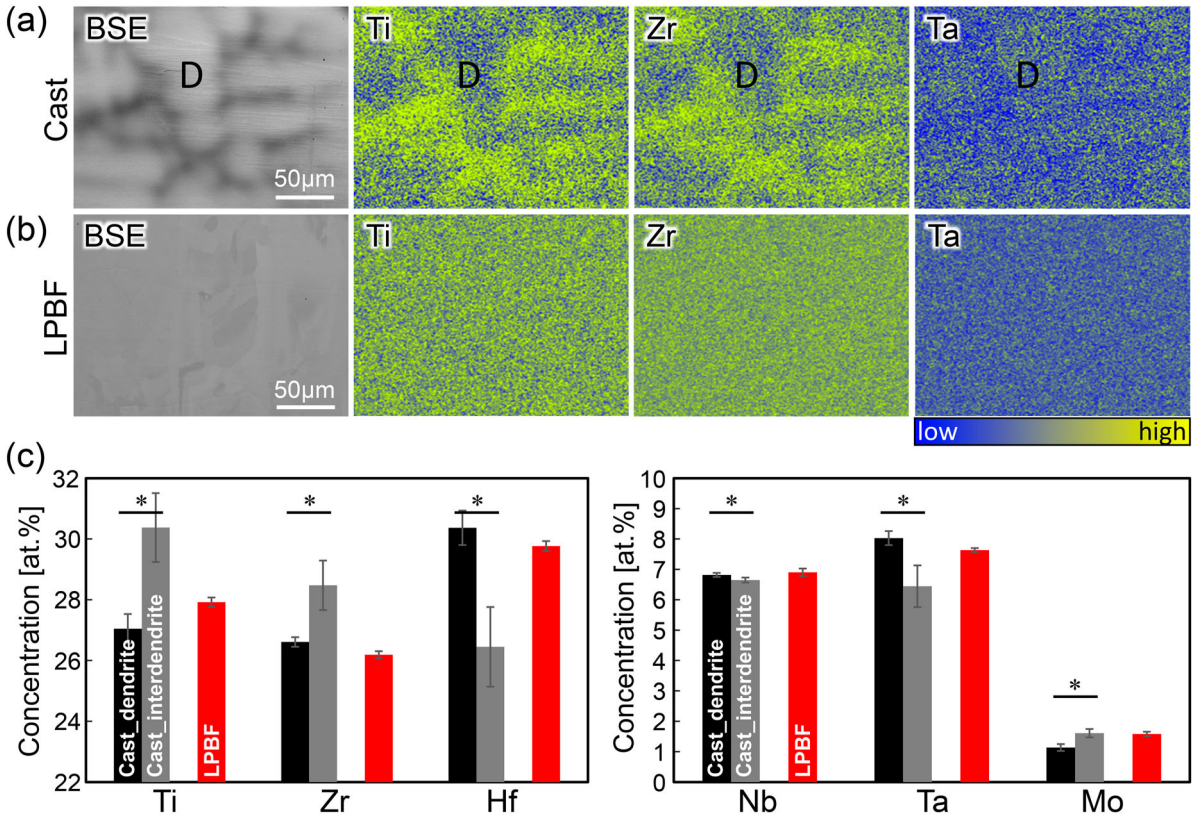

Figure 2. Compositional distribution analyses. BSE images and EDS maps for Ti, Zr, and Ta of (a) LPBF-built and (b) cast $Ti_{28.33}Zr_{28.33}Hf_{28.33}Nb_{6.74}Ta_{6.74}Mo_{1.55}$ BioHEA specimen. (c) Concentrations of constituent elements in the dendrite and inter-dendrite regions of the cast specimen and LPBF specimen determined by EDS. $*$: $P < 0.05$.

Figure 3(a) presents the inverse pole figure maps taken in the *x*-, *y*-, and *z*-axes, representing the developed distinctive crystallographic textures depending on the scan speed. Figure 3(b) shows the corresponding 001 pole figures, and the orientation degree of $<001>$ along the build (*z*-) direction is shown in Figure 3(c). Specimen V_{1000} showed an intense single crystalline-like crystallographic texture where $<001>$ was strongly oriented along the *x*-, *y*-, and *z*-directions (the so-called cube texture), which is a typical texture that evolves under the Scan strategy XY adopted in this study [28]. The crystallographic orientation was inherited across multiple layers along the *z*-axis (Figure 3(a1)); the layer thickness was 60 μm. This indicates that epitaxial growth at the melt-pool boundaries plays an important role in the intense crystallographic textures. Once the cube texture is stabilised, epitaxial growth facilitates the inheritance of the crystal orientation in both laser scans in the *x*- and *y*-directions. Consequently, grain boundaries with large misorientations were eliminated, resulting in a single crystalline-like texture. In other words, the reduction in grain boundary energy would be the driving force behind the stabilisation of the cube texture. In our previous study, a bimodal microstructure was developed in which fine equiaxed grains formed along the melt pool bottom that intercepted epitaxial growth between the melt pool tracks and between the layers; hence, single crystalline formation was not achieved [12]. This phenomenon was attributed to a difference in the melting point based on elemental segregation, which was a challenge to overcome. $Ti_{28.33}Zr_{28.33}Hf_{28.33}Nb_{6.74}Ta_{6.74}Mo_{1.55}$ BioHEA in this study successfully achieved a single crystalline-like texture by markedly suppressing segregation.

With increasing laser scanning speed, the texture intensity significantly decreased, and a polycrystalline structure with an almost random orientation was obtained in specimen V_{1600}. This is closely related to the solidification condition expressed by the relationship between the thermal gradient (G) and migration rate of the solid–liquid interface (R). It has been reported that R increases with an increase in scanning speed, whereas G changes insignificantly [18,29]. Polycrystalline formation at high scanning speeds could be due to the increased degree of compositional undercooling owing to the decrease in G/R, and this trend of texture change is consistent with previous reports for ordinary alloys [18].

Figure 4(a) shows the yield stress of the cast and LPBF-fabricated BioHEAs accompanied by fracture strain. The cast specimens did not fracture under compression.

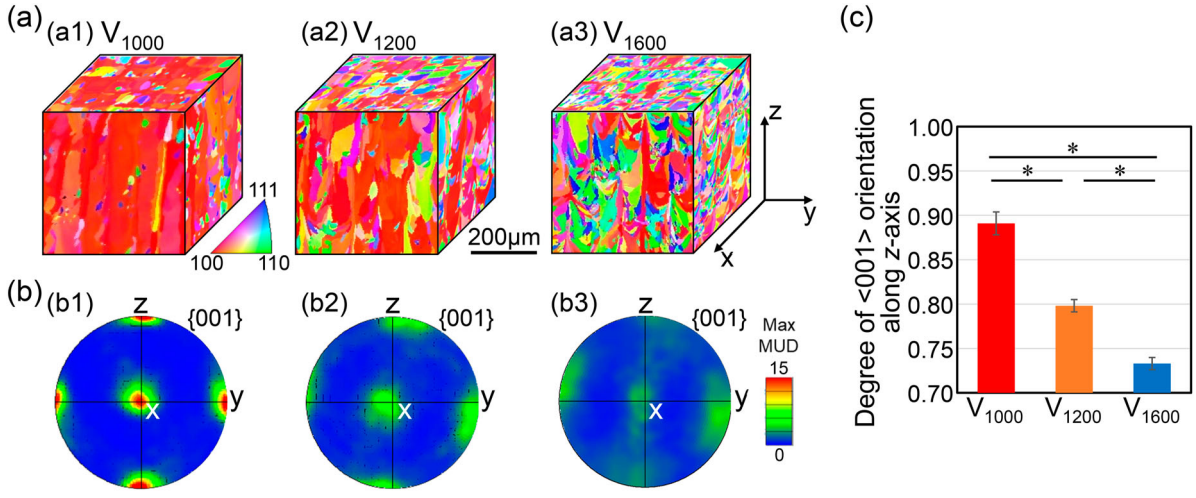

Figure 3. Crystallographic texture of the LPBF-built specimens. (a) Inverse pole figure maps taken in the orthogonal three planes and (b) the corresponding 001 pole figures. (c) Quantified degree of $<001>$ crystallographic orientation along z-axis. $*$: $P < 0.05$.

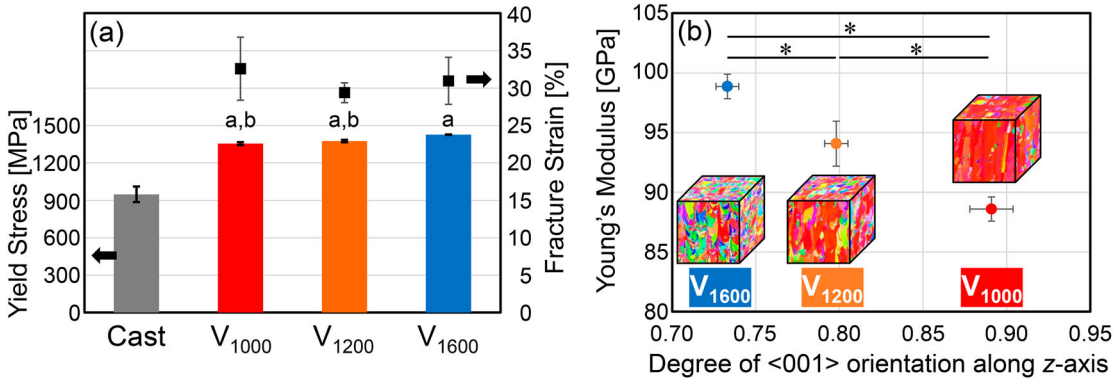

Figure 4. Mechanical properties of the BioHEA: (a) Yield stress and fracture strain and (b) Young's modulus of the cast and LPBF-built $Ti_{28.33}Zr_{28.33}Hf_{28.33}Nb_{6.74}Ta_{6.74}Mo_{1.55}$ BioHEA specimen; $*$: $P < 0.05$ by Tukey's test; a: $P < 0.05$ vs cast; b: $P < 0.05$ vs V_{1600} by t-test.

The LPBF specimens exhibited a fracture strain of approximately 30%, indicating high ductility. The yield stress of the cast specimen reached 949 MPa, while LPBF processing led to a significant improvement in the yield stress, reaching 1355–1426 MPa, 1.4–1.5 times greater than that of the cast specimen. The higher yield stress in specimen V_{1600} than in V_{1000} and V_{1200} is because of the grain boundaries (Hall-Petch effect). However, the strengthening effect of the LPBF fabrication itself is much greater than that, which could be due to the enhanced solid solution strengthening in the heavily distorted lattice [30], effectively achieved by suppressing elemental segregation, thus realising a super-solid solution. These benefits were obtained by LPBF-specific ultrarapid cooling.

Figure 4(b) shows the Young's modulus of the LPBF-processed BioHEA as a function of the $<001>$ orientation degree. The lowest Young's modulus (88.6 GPa) was observed for specimen V_{1000}, which had the highest degree of $<001>$ orientation and the most prominent single crystalline-like texture. Young's modulus increased as the degree of the $<001>$ orientation decreased. This indicates that this BioHEA exhibits anisotropy in Young's modulus depending on the crystallographic direction, as in Ti-15Mo-5Zr-3Al [20] and Ti-29Nb-Ta-Zr [22], which exhibit an unstable β-phase. The modulus of the LPBF-fabricated BioHEA was lower than those of CP-Ti ($\sim$110 GPa) and SUS316L ($\sim$200 GPa). Further reduction of e/a toward four may increase BCC instability, and further lower Young's modulus, as observed in Ti-based alloys. However, the relationship between BCC phase stability and elastic modulus for multi-component BioHEAs needs to be clarified in the future to create highly functional metal biomaterials for orthopaedic applications.

Figure 5 shows the biocompatibility of the LPBF-fabricated BioHEA together with that of the cast specimen, CP-Ti, and SUS316L. Osteoblast density (Figure 5(a)) adhered to the specimens was evaluated using Giemsa staining (Figure 5(b)). The cell density of the LPBF-fabricated BioHEA was comparable to that of the cast material and CP-Ti and was significantly higher

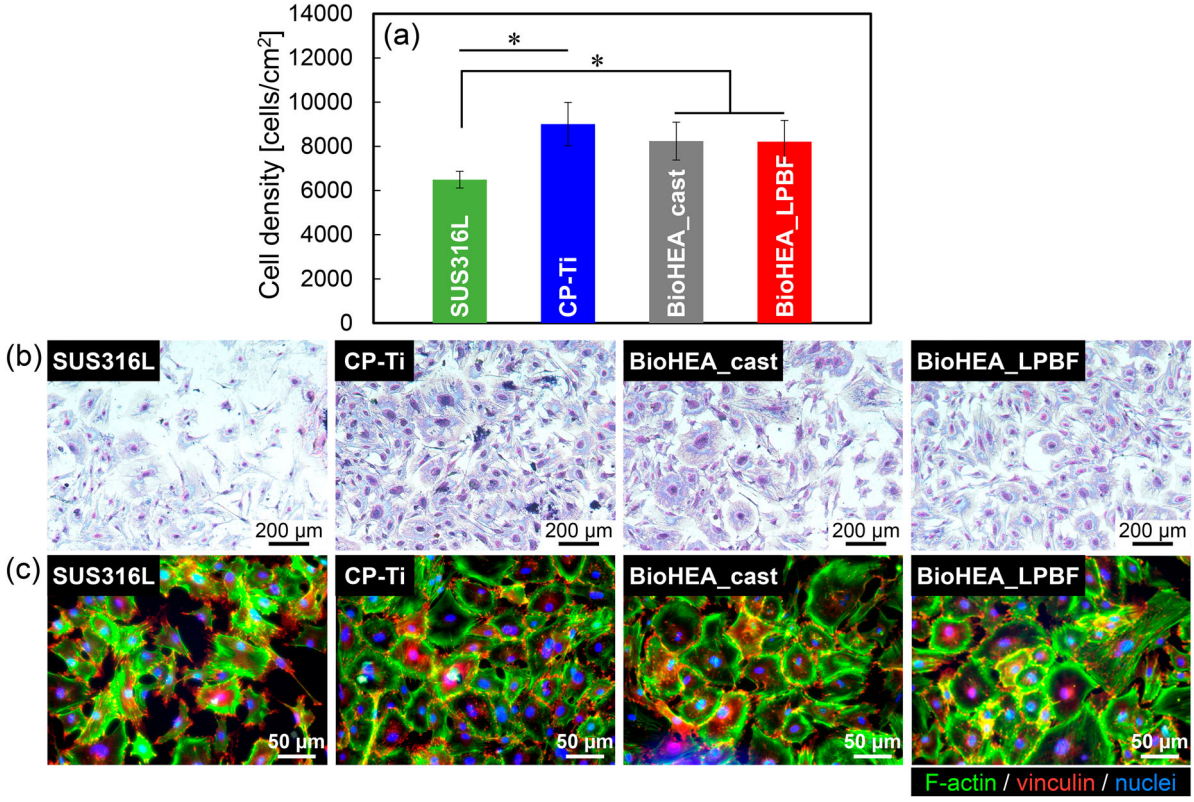

Figure 5. Biocompatibility of LPBF-fabricated $Ti_{28.33}Zr_{28.33}Hf_{28.33}Nb_{6.74}Ta_{6.74}Mo_{1.55}$ BioHEA in comparison with cast specimen, CP-Ti, and SUS316L. (a) Quantitative analysis of cell density; $*$: $P < 0.05$. (b) Giemsa and (c) fluorescent staining images of osteoblasts adhesion on the specimens.

than that of SUS316L. Figure 5(c) shows fluorescent images of cytoskeletal components and focal adhesion of osteoblasts adhered to the specimens. Osteoblasts on SUS316L were observed to shrink in size with poor cytoskeletal organisation. In contrast, osteoblasts on CP-Ti, cast BioHEA, and LPBF-processed BioHEA exhibited a widespread morphology with a dense network of actin fibres. Furthermore, compositional segregation in BioHEA has been shown to reduce the cell spreading area [12], which is essential for osteogenic differentiation [31].

4. Conclusion

In conclusion, our strategy, that is, the combination of (a) compositional design that reduces the difference between liquidus and solidus temperatures and valence electron concentration (e/a), and (b) LPBF technology that enables segregation suppression (formation of super-solid solution) owing to ultra-rapid solidification and crystallographic texture control, which cannot be achieved by other methods, resulted in the creation of a promising BioHEA with a low modulus, excellent strength-ductility balance, and good cytocompatibility, all of which are essential for biomaterials. In addition, the LPBF offers the added value of patient-specific shape customisability. Thus, the LPBF-fabricated TiZrHfNbTaMo BioHEA has great potential as a next-generation metallic biomaterial with multiple advantages.

Disclosure statement

No potential conflict of interest was reported by the author(s).

Funding

This work was supported by CREST-Nanomechanics: Elucidation of macroscale mechanical properties based on understanding nanoscale dynamics for innovative mechanical materials [grant number JPMJCR2194] from the Japan Science and Technology Agency (JST).

Data availability statement

Data will be made available on request.

ORCID

Ozkan Gokcekaya http://orcid.org/0000-0002-9258-858X
Takuya Ishimoto http://orcid.org/0000-0003-0081-0591
Aira Matsugaki http://orcid.org/0000-0002-8427-7124
Ryosuke Ozasa http://orcid.org/0000-0002-2773-072X
Markus Weinmann http://orcid.org/0000-0002-9029-7535

Christoph Schnitter http://orcid.org/0000-0001-5488-1737
Melanie Stenzel http://orcid.org/0000-0002-6357-1391
Hyoung Seop Kim http://orcid.org/0000-0002-3155-583X
Yoshitsugu Miyabayashi http://orcid.org/0000-0002-9134-9149
Takayoshi Nakano http://orcid.org/0000-0001-8052-1698

References

[1] Liu YJ, Li SJ, Wang HL, et al. Microstructure, defects and mechanical behavior of beta-type titanium porous structures manufactured by electron beam melting and selective laser melting. Acta Mater. 2016;113:56–67.
[2] Zhang Y, Zuo TT, Tang Z, et al. Microstructures and properties of high-entropy alloys. Prog Mater Sci. 2014;61:1–93.
[3] Tsai M-H, Yeh J-W. High-entropy alloys: a critical review. Mater Res Lett. 2014;2:107–123.
[4] Todai M, Nagase T, Hori T, et al. Novel TiNbTaZrMo high-entropy alloys for metallic biomaterials. Scr Mater. 2017;129:65–68.
[5] Nagase T, Todai M, Hori T, et al. Microstructure of equiatomic and non-equiatomic Ti-Nb-Ta-Zr-Mo high-entropy alloys for metallic biomaterials. J Alloys Compd. 2018;753:412–421.
[6] Nagase T, Mizuuchi K, Nakano T. Solidification microstructures of the ingots obtained by arc melting and cold crucible levitation melting in TiNbTaZr medium-entropy alloy and TiNbTaZrX (X = V, Mo, W) high-entropy alloys. Entropy. 2019;21:483.
[7] Hori T, Nagase T, Todai M, et al. Development of non-equiatomic Ti-Nb-Ta-Zr-Mo high-entropy alloys for metallic biomaterials. Scr Mater. 2019;172:83–87.
[8] Nagase T, Iijima Y, Matsugaki A, et al. Design and fabrication of Ti–Zr-Hf-Cr-Mo and Ti–Zr-Hf-Co-Cr-Mo high-entropy alloys as metallic biomaterials. Mater Sci Eng C. 2020;107:110322.
[9] Yuan Y, Wu Y, Yang Z, et al. Formation, structure and properties of biocompatible TiZrHfNbTa high-entropy alloys. Mater Res Lett. 2019;7:225–231.
[10] Motallebzadeh A, Peighambardoust NS, Sheikh S, et al. Microstructural, mechanical and electrochemical characterization of TiZrTaHfNb and $Ti_{1.5}ZrTa_{0.5}Hf_{0.5}Nb_{0.5}$ refractory high-entropy alloys for biomedical applications. Intermetallics. 2019;113:106572.
[11] Yang W, Pang S-J, Wang G, et al. Ti–Zr–Hf–Nb–Ta–Sn high-entropy alloys with good properties as potential biomaterials. Rare Met. 2022;41:2305–2315.
[12] Ishimoto T, Ozasa R, Nakano K, et al. Development of TiNbTaZrMo bio-high entropy alloy (BioHEA) supersolid solution by selective laser melting, and its improved mechanical property and biocompatibility. Scr Mater. 2021;194:113658.
[13] Torralba JM, Alvaredo P, García-Junceda A. High-entropy alloys fabricated via powder metallurgy. A critical review. Powder Metall. 2019;62:84–114.
[14] Zhang F, Tong Y, Jin K, et al. Chemical complexity induced local structural distortion in NiCoFeMnCr high-entropy alloy. Mater Res Lett. 2018;6:450–455.
[15] DebRoy T, Wei HL, Zuback JS, et al. Additive manufacturing of metallic components – process, structure and properties. Prog Mater Sci. 2018;92:112–224.
[16] Li J, Cheng T, Liu Y, et al. Simultaneously enhanced strength and ductility of Cu-15Ni-8Sn alloy with periodic heterogeneous microstructures fabricated by laser powder bed fusion. Addit Manuf. 2022;54:102726.
[17] Ishimoto T, Hagihara K, Hisamoto K, et al. Crystallographic texture control of beta-type Ti–15Mo–5Zr–3Al alloy by selective laser melting for the development of novel implants with a biocompatible low Young's modulus. Scr Mater. 2017;132:34–38.
[18] Gokcekaya O, Ishimoto T, Hibino S, et al. Unique crystallographic texture formation in Inconel 718 by laser powder bed fusion and its effect on mechanical anisotropy. Acta Mater. 2021;212:116876.
[19] Hagihara K, Nakano T. Control of anisotropic crystallographic texture in powder bed fusion additive manufacturing of metals and ceramics—a review. JOM. 2022;74:1760–1773.
[20] Tane M, Akita S, Nakano T, et al. Low young's modulus of Ti–Nb–Ta–Zr alloys caused by softening in shear moduli c′ and c44 near lower limit of body-centered cubic phase stability. Acta Mater. 2010;58:6790–6798.
[21] Feuerbacher M, Würtz E, Kovács A, et al. Single-crystal growth of a FeCoCrMnAl high-entropy alloy. Mater Res Lett. 2017;5:128–134.
[22] Tane M, Akita S, Nakano T, et al. Peculiar elastic behavior of Ti–Nb–Ta–Zr single crystals. Acta Mater. 2008;56:2856–2863.
[23] Okugawa M, Ohigashi Y, Furishiro Y, et al. Equiaxed grain formation by intrinsic heterogeneous nucleation via rapid heating and cooling in additive manufacturing of aluminum-silicon hypoeutectic alloy. J Alloys Compd. 2022;919:165812.
[24] Sheikh S, Shafeie S, Hu Q, et al. Alloy design for intrinsically ductile refractory high-entropy alloys. J Appl Phys. 2016;120:164902.
[25] Yang T, Zhao YL, Liu WH, et al. Ductilizing brittle high-entropy alloys via tailoring valence electron concentrations of precipitates by controlled elemental partitioning. Mater Res Lett. 2018;6:600–606.
[26] Iijima Y, Nagase T, Matsugaki A, et al. Design and development of Ti–Zr–Hf–Nb–Ta–Mo high-entropy alloys for metallic biomaterials. Mater Des. 2021;202:109548.
[27] Gokcekaya O, Ishimoto T, Todo T, et al. Influence of powder characteristics on densification via crystallographic texture formation: Pure tungsten prepared by laser powder bed fusion. Addit Manuf Lett. 2021;1:100016.
[28] Gokcekaya O, Hayashi N, Ishimoto T, et al. Crystallographic orientation control of pure chromium via laser powder bed fusion and improved high temperature oxidation resistance. Addit Manuf. 2020;36:101624.
[29] Karayagiz K, Johnson L, Seede R, et al. Finite interface dissipation phase field modeling of Ni–Nb under additive manufacturing conditions. Acta Mater. 2020;185:320–339.
[30] Yin B, Curtin WA. Origin of high strength in the CoCrFeNiPd high-entropy alloy. Mater Res Lett. 2020;8:209–215.
[31] Yang Y, Wang X, Wang Y, et al. Influence of cell spreading area on the osteogenic commitment and phenotype maintenance of mesenchymal stem cells. Sci Rep. 2019;9:6891.